

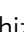




Effect of chemically induced permittivity changes on the plasmonic properties of metal nanoparticles

Noboru Saito^{1,7}, Sou Ryuzaki^{1,2,7}[✉], Yuta Tsuji¹, Yutaka Noguchi³, Rintaro Matsuda¹, Pangpang Wang⁴, Daisuke Tanaka⁵, Yusuke Arima¹, Koichi Okamoto⁶, Kazunari Yoshizawa¹ & Kaoru Tamada¹[✉]

Understanding chemical effects on the plasmonic properties of a metal nanomaterial due to the surface molecules on that metal is of great importance in the field of plasmonics and these effects have yet to be completely elucidated. Here, we report mechanisms of the chemically induced change in the electronic state at the metal-ligand interface of silver nanoparticles due to the ligand molecules, and the effect of this change on the plasmonic properties of those nanoparticles. It was found that changes in the electron density of states at the metal-ligand interface cause alterations in the induced and permanent dipole moments, and eventually to the permittivity at the interface, when the wave function near the Fermi level is localized at the interface. These alterations play a key role in determining the plasmonic properties of silver nanoparticles. The present findings provide a more precise understanding of the interconnection between the electronic states at the metal-organic interface and the plasmonic properties of the metal.

¹Institute for Materials Chemistry and Engineering, Kyushu University, Fukuoka, Japan. ²PRESTO, Japan Science and Technology Agency (JST), Saitama, Japan. ³Department of Science and Technology, Meiji University, Kawasaki, Japan. ⁴Institute of Systems, Information Technologies and Nanotechnologies (ISIT), Fukuoka, Japan. ⁵Department of Electrical and Electronic Engineering, National Institute of Technology, Oita College, Oita, Japan. ⁶The Institute of Scientific and Industrial Research, Osaka University, Osaka, Japan. ⁷These authors contributed equally: Noboru Saito, Sou Ryuzaki. ✉email: ryuzaki@ms.ifoc.kyushu-u.ac.jp; tamada@ms.ifoc.kyushu-u.ac.jp

The initiation of changes in the localized surface plasmon resonance (LSPR) properties of plasmonic nanomaterials by the chemical bonding of organic molecules to their surface is one of the most important photochemical research objects for both fundamental and applied science. Therefore, understanding this object will not only provide us with more choices for controlling LSPR properties but also increase flexibility when designing plasmonic devices^{1–6}. Recently, surface molecules on a plasmonic metal nanomaterial have been reported to cause an additional damping and density alteration of the free electrons in the metal via changes in the electronic state at the metal–organic interface, and these changes are caused by chemical interactions between the metal and surface molecules^{7–10}. The additional damping, called chemical interface damping (CID), is induced by interactions between the electron wave functions localized at the metal–organic interface and the free electrons that contribute to the LSPR, thereby resulting in LSPR decay because of an increased scattering rate of the free electrons^{7–9}. Thus, the CID effect basically provides a decrease and increase in the peak intensity and full-width at half maxima (FWHM), respectively, in a plasmon resonance spectrum. Moreover, an alteration in the free electron density in metal can be caused via an energy level alignment between the electronic states of the metal and the surface molecules at the interface, and/or via a spill-out of the electrons contributing LSPR in the core metal to the ligand molecules^{10,11}. As the density of free electrons directly contributes to determining the plasmon frequency, the electron density alteration results in a peak shift in the LSPR in the plasmon resonance spectrum. Recent works have expanded the understanding of these effects on LSPR properties due to chemically induced changes in the electronic states at the metal–organic interface^{7–12}. However, these works do not take into account a change in dipole moments at the interface due to the chemical interactions between the metal and organic molecules, despite the fact that the localized dipole moment is recognized to be a critical factor for determining the LSPR properties. Here, both the permanent and induced dipole moments should be taken into account, because the metal–organic interface is situated in a plasmonic electric field around the surface of a plasmonic metal nanomaterial. Therefore, it is important to precisely determine the roles of the localized dipole moment at the metal–organic interface on the LSPR properties of plasmonic nanomaterials to further understand the mechanism underlying plasmon resonances in the presence of different electronic states at the interface.

In this study, we report a chemically induced change in the localized dipole moments at the metal–organic interface and how these changes affect the plasmonic properties of metal nanomaterials qualitatively. It was found that changes in the electron density of states (DOS) at the metal–organic interface due to the surface molecules cause alterations in the localized dipole moments and finally in permittivity at the interface, and these alterations are involved in determining the plasmonic properties. Two kinds of Ag nanoparticles with myristate and thiolate/dithiolate ligands are employed in this study, and changes in the electron DOS and permittivity, which depends on the dipole moment, at the interface before and after ligand displacements are examined by measuring the tunneling currents and activation energies of single-electron transport between nanoparticles, respectively. In addition, these physical properties are theoretically investigated by first-principles calculations. The causality between the DOS and the localized dipole moments at the metal–ligand interface and the roles of the localized dipole moments on the LSPR properties of Ag nanoparticles are finally discussed. In addition, the CID effect in each nanoparticle is discussed by measuring the complex dielectric functions by ellipsometry.

Results and discussion

Experimental evaluation of the localized dipole moments. To discuss the effects on the LSPR properties of Ag nanoparticles due to changes in the localized dipole moments at the metal–ligand interface, three kinds of Ag nanoparticle monolayer films capped with different ligands: (i) myristate (AgMy)^{13,14}, (ii) 1-tetradecanethiol (AgSC), which has the same number of carbon atoms as myristate; and (iii) 1,16-hexadecanidithiol (AgDT), which provided cross-linked molecular structures between the nanoparticles, were prepared by the immersion method (Fig. 1a–c). As the plasmon resonance spectrum of nanoparticle films depends on the metal type, particle size, neighboring interparticle distance, and ligand refractive index, these factors must be the same for each nanoparticle film to discuss only the effects of the change in the localized dipole moments¹⁵. Thus, the above three kinds of ligands, with almost the same refractive index, and the immersion method, which provides ca. 85% ligand displacements, while maintaining the interparticle distance, were employed in this study (see “Methods”)¹⁶. Indeed, the same particle size (radius $r = 2.4$ nm) and interparticle distance (edge-to-edge $d = 1.9$ nm) are observed in the scanning electron microscopy (SEM) and transmission electron microscopy (TEM) images, as shown in Fig. 1d–f.

Interestingly, only the AgMy (blue) films show a decidedly different plasmon resonance spectrum with a shorter resonance wavelength, larger intensity, and narrower FWHM compared with those of the AgSC (red) and AgDT (green) films (Fig. 1g); this result occurs despite each film having the same value of the above four factors (metal type, particle size, neighboring interparticle distance, and ligand refractive index). Therefore, an alteration in the free electron density in the core metal, which is caused by effects of the energy level alignment and/or the spill-out, due to the ligand displacements is potentially a contributor to the difference in the spectra. However, it is unreasonable to explain the difference in the spectral properties among these Ag nanoparticle films by only the electron density alteration. If the difference in the spectra is caused only by an alteration in the density of the free electrons, the spectral area, which is equal to the integrated spectrum, should be different among them, because the total number of electrons (N) can be described as below¹⁷,

$$N = \sum f \quad (1)$$

$$f \propto \int \alpha_e(\nu) d\nu. \quad (2)$$

Here, f , α_e , and ν denote the oscillator strength, the molar extinction coefficient, and the wavenumber ($1/\lambda$), respectively. However, the spectral area is almost the same for each film: 172.6, 182.5, and 172.4 for AgMy, AgSC, and AgDT, respectively. Therefore, the other factors, such as the change in the localized dipole moments and/or CID, contribute to the differences in the plasmon resonance spectra shown in Fig. 1g.

The dipole moments reflecting the DOS affect the permittivity. Thus, we measured Arrhenius plots of conductivity (σ), because the activation energy (E_a) and tunneling current between nanoparticles, which depend on the permittivity and the DOS near the Fermi level, respectively, can be estimated by these plots^{18–20}. In the thermal hopping mechanism, conductivity can be described with E_a as follows:

$$\sigma \propto \exp\left(-\frac{E_a}{k_B T}\right). \quad (3)$$

Here, k_B is the Boltzmann constant and T is the temperature. The Arrhenius plots of AgMy (blue), AgSC (red), and AgDT (green) films reveal that E_a significantly depends on the anchor atoms of the ligands (Fig. 1h). Although a carbon chain is the

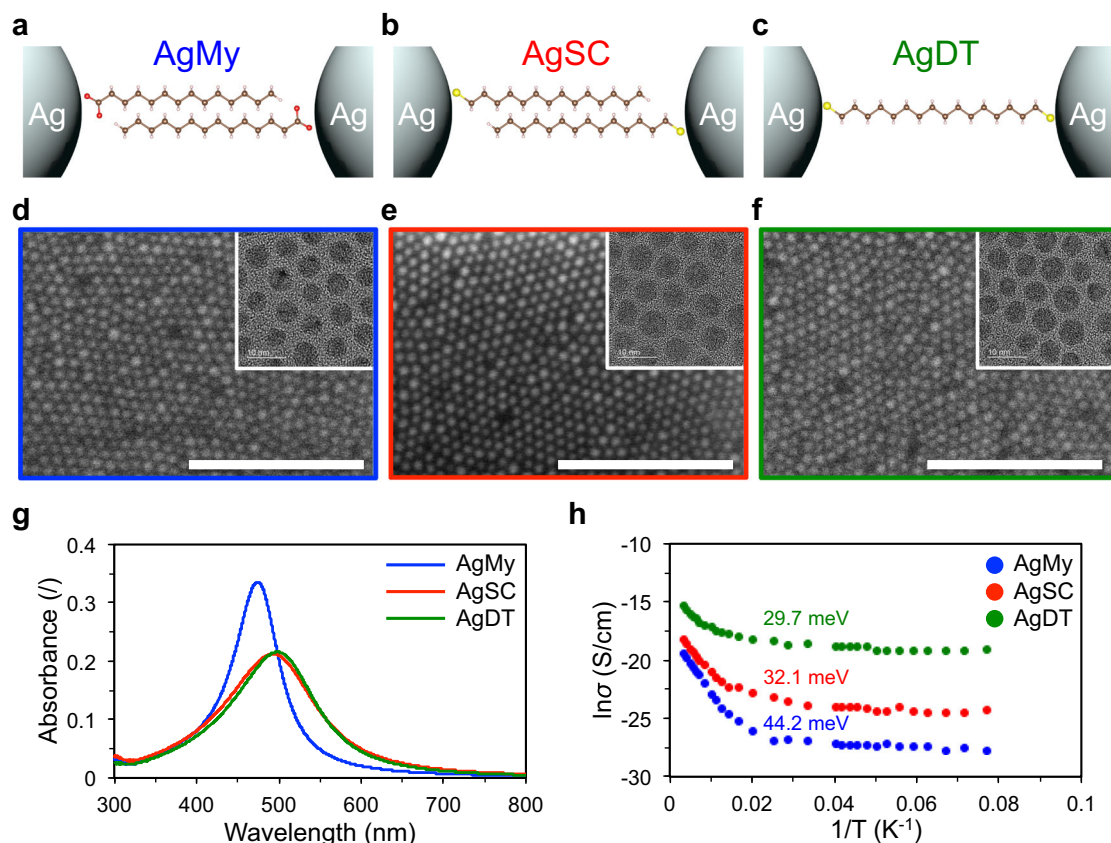


Fig. 1 Physical properties of AgMy, AgSC, and AgDT films. **a–c** Schematic illustrations of each ligand: **a** myristate (My), **b** 1-tetradecanethiol (SC), and **c** 1,16-hexadecanedithiol (DT). **d–f** SEM images of each Ag nanoparticle monolayer film: **d** AgMy, **e** AgSC, and **f** AgDT. Scale bars correspond to 100 nm and the inset figures are TEM images of each film. For all films, the same particle size (radius $r = 2.4$ nm) and interparticle distance (edge-to-edge $d = 1.9$ nm) are observed, because the immersion method provides ligand displacements, while maintaining the interparticle distance in a film. **g** Plasmon resonance spectra of the AgMy (blue), AgSC14 (red), and AgDT16 (green) monolayer films. **h** Arrhenius plots of conductivity for the AgMy (blue), AgSC14 (red), and AgDT16 (green) monolayer films. Details of how to estimate E_a are described in the Supplementary Information (see Supplementary Fig. 1).

main part of the ligands for all three nanoparticles, the E_a of the AgMy (44.2 meV) film is a remarkably higher value than that of AgSC (32.1 meV) and AgDT (29.7 meV) (see Supplementary Fig. 1). As the activation energy E_a corresponds to the minimum energy required for overcoming the energy barrier of single-electron transport between nanoparticles, both the electronic states of the metal–ligand interface and the ligand bodies contribute E_a values. However, in this study, because the anchor atom is oxygen in AgMy nanoparticles, whereas the anchor atom is sulfur in AgSC and AgDT nanoparticles, the relatively high E_a value of AgMy films can be mainly attributed to the electronic states of the Ag–O interface. Here, E_a is interrelated to permittivity $\epsilon_r \epsilon_0$ between Ag nanoparticles, where ϵ_r and ϵ_0 are the relative and vacuum permittivity, respectively, as described in the following equations with the capacitance (C), the elementary charge (e) particle radius (r), and edge-to-edge interparticle distance (d)²¹,

$$E_a = \frac{e^2}{2C}, \quad (4)$$

$$C = 4\pi\epsilon_r\epsilon_0 \left(\frac{1}{r} - \frac{1}{r+d} \right)^{-1} \quad (5)$$

Therefore, the present results suggest that the permittivity of the Ag–O interface is smaller than that of the Ag–S interface. On the other hand, the tunneling currents show different values for each film and the AgMy film shows the smallest conductance of

the three (Fig. 1h). In the low-temperature region (below 25 K, $1/T = 0.04$) of the Arrhenius plots, each conductivity value is independent of temperature, indicating that the tunneling current is the dominant conduction mechanism in this temperature region (Fig. 1h). As the tunneling current is proportional to the local DOS near the Fermi level, the lower tunneling conductance in the AgMy film indicates a lower DOS near the Fermi level at the metal–ligand interface compared with that of the AgSC film, because the two ligands have the same structure but different anchor atoms. Further details of the conduction mechanism are discussed in the Supplementary Information (see Supplementary Fig. 2).

The plasmon resonance spectra and the Arrhenius plots for AgMy, AgSC, and AgDT films revealed three facts as follows: (i) the Ag–O interface causes a shorter resonance wavelength, higher intensity, and narrower FWHM in its plasmon resonance spectrum compared with those of the Ag–S interface; (ii) the permittivity of the Ag–O interface is smaller than that of the Ag–S interface; and (iii) the DOS near the Fermi level at the Ag–O interface is lower than that of the Ag–S interface. We next discuss the relations among the three facts via first-principles calculations of the electronic states in AgMy and AgSC nanoparticles.

Theoretical evaluation of the localized dipole moments. For AgMy and AgSC films, the nanoparticle distance is $d = 1.9$ nm, which is comparable to the molecular length of each ligand. Therefore, the unit model consisting of two interdigitated

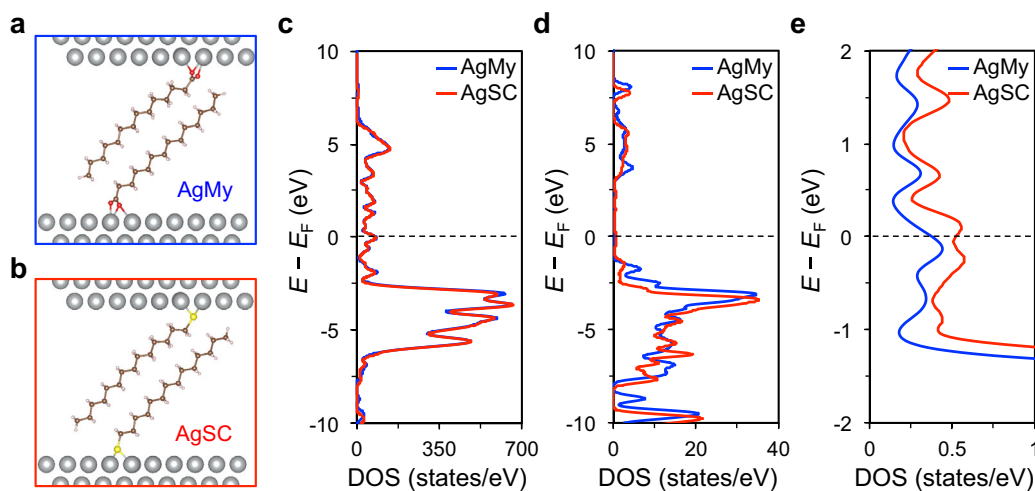


Fig. 2 Comparison of the electron density of states (DOS) between AgMy and AgSC. **a, b** Optimized structures of the slab model for the calculations: **a** AgMy and **b** AgSC. **c** DOS values of the whole atomic model (total DOS values) of AgMy (blue) and AgSC (red). These DOS values appear to be almost overlapping, because electrons from the Ag atoms are numerically in a majority and are dominant. **d** DOS values projected for the ligand part of AgMy (blue) and AgSC (red). These DOS values are also almost the same, because the two ligands have the same structure, except for their terminal groups. **e** Expanded DOS values for the ligand part of AgMy (blue) and AgSC (red) in the range of -2 to 2 eV. These DOS values are present near the Fermi level because of chemical interactions between the Ag surface and ligands; in addition, the DOS near the Fermi level of AgMy is lower than that of AgSC.

molecules between Ag nanoparticles, as shown in Fig. 2a, b, is reasonable to discuss the DOS, the localized dipole moments, and the permittivity between the Ag nanoparticles. Thus, the DOS of the unit model consisting of Ag–ligand–ligand–Ag were calculated. However, as the actual structure between the Ag nanoparticles is a much more complex interface, this point should be studied in detail in the future. The total DOS values for the whole optimized slab models of AgMy and AgSC nanoparticles were found to be almost the same (Fig. 2c), because the main energy level distributed between $E - E_F = -2$ and -6 eV corresponds to the d -band of Ag atoms. Here, E and E_F denote the energy level and Fermi level, respectively. The two ligands have the same structure, except for their terminal groups; the DOS values projected for both ligands also show a similar distribution and reflect their gap of the highest occupied and the lowest unoccupied molecular orbital (Fig. 2d). Indeed, the main DOS values distributed in the range of -2 to -10 eV, as shown in Fig. 2d, correspond to carbon chains (see Supplementary Fig. 3). Notably, the present calculations reveal the presence of DOS values near the Fermi level that are caused by chemical interactions between the Ag surface and ligands; in addition, the DOS near the Fermi level (-1 to 1 eV) of AgMy is lower than that of AgSC (Fig. 2e). This difference in the DOS values seems to be the main factor causing the difference in the plasmon resonance spectra between AgMy and AgSC, because the free electrons in the vicinity of the Fermi level play a role as valence electrons in the determination of physical properties.

Molecular orbitals near the Fermi level generally provide important information for understanding the physical properties of the object. In the cases of both AgMy and AgSC nanoparticles, the wave functions around the Fermi level (-0.1 to 0.1 eV) are localized around the anchor atoms, although the wave functions are mostly distributed in Ag atoms (Fig. 3a, b). The partial DOS (PDOS) values of the anchor atoms clearly show that O atoms have lower electron density than that of S atoms near the Fermi level, even though the DOS intensity of the O atoms looks larger than that for the S atoms in the whole range from -10 to 10 eV (Fig. 3c, d). These calculation results are consistent with the experimental results discussed in Fig. 1; namely, the DOS near the Fermi level at the Ag–O interface is thus experimentally and

theoretically found to be lower than that of the Ag–S interface. In a comparison of single O and S atoms, the difference in PDOS values is much more noticeable (Fig. 3e). Here, a different molecular length for each ligand potentially causes the PDOS difference shown in Fig. 3. However, the main factor causing the PDOS difference is the anchor atom, because Ag nanoparticles capped with 1-tridecanethiol (AgSC13), which has the same molecular length as AgMy, show nearly identical PDOS values as AgSC (see Supplementary Fig. 4) and PDOS properties of AgDT also indicates almost the same as that of AgSC (see Supplementary Fig. 5). In a qualitative manner, a small number of electrons near the Fermi level, i.e., valence electrons, can cause a small dipole moment and a small permittivity when the electronic band structures are almost the same between comparison molecules, because the dipole moment μ and the relative permittivity ϵ_r can be respectively described by

$$\mu = Ql, \quad (6)$$

$$\epsilon_r = 1 + \frac{N_D e^2}{m \epsilon_0} \sum_i \frac{f_i}{\omega_i^2 - \omega^2 - i\omega\gamma_i}. \quad (7)$$

Here, Q , l , N_D , m , f_i , ω_i , and γ_i denote magnitude of the charge, distance between charges, the electron density, the electron mass, the oscillator strength, the resonant frequency, and the damping coefficient, respectively, for the i th type of electron. In this study, as the electronic band structure of My molecules in AgMy is almost the same to that of SC molecules in AgSC (Fig. 2d) and the electron density near the Fermi level in My molecules is lower than that in SC molecules (Figs. 2 and 3), the dipole moment and the permittivity of My molecules on the Ag nanoparticle is qualitatively assumed to be lower than those of SC molecules.

The polarizability (α), which is involved in the induced dipole moment (μ_i), the permanent dipole moment (μ_p) of the constituent molecules, contribute to the polarization (P) of the molecules. To consider the above speculation and how the dipole moments contribute to the permittivity of the molecules, the relation between the dipole moments and the permittivity for

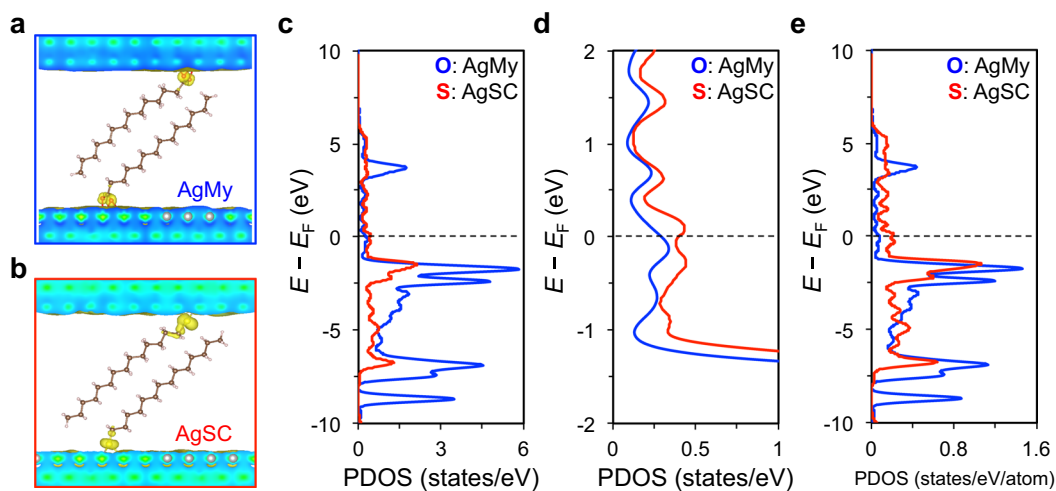
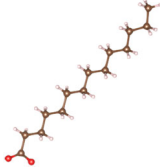
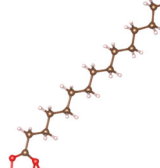
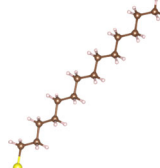
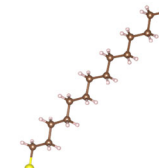


Fig. 3 Comparison between the electron partial density of states (PDOS) projected only for the O atom in AgMy and only for the S atom in AgSC. **a, b** Isosurfaces of the band decomposed charge density around the Fermi level (the squared wave function integrated from -0.1 to 0.1 eV) calculated for **a** AgMy and **b** AgSC. The isovalue was set to 0.0005 in both systems. Each wave function is found to be localized at the interface between the anchor atoms and the surface. **c** PDOS values projected only for the O atoms in AgMy (blue) and only for the S atom in AgSC (red). On the whole, the PDOS of the O atoms exhibits a higher value than that of the S atom in the range from -10 to 10 eV. **d** Expanded PDOS values for the O atom in AgMy (blue) and the S atom in AgSC (red) in the range from -2 to 2 eV. These PDOS values clearly indicate that the difference in the DOS near the Fermi level between AgMy and AgSC shown in Fig. 2e is attributed to the anchor atoms. **e** PDOS values per atom for the O atom in AgMy (blue) and the S atom in AgSC (red). The difference in the PDOS values is much more noticeable.

Table 1 Calculated physical parameters of My and SC molecules with and without Ag atoms.

	My	AgMy	SC	AgSC
Structure				
Polarizability α [$C \cdot m^2 \cdot V^{-1}$]	2.64×10^{-39}	4.97×10^{-39}	2.88×10^{-39}	5.66×10^{-39}
Dipole moment μ_p [$C \cdot m$]	1.18×10^{-28}	2.64×10^{-30}	1.30×10^{-28}	8.87×10^{-30}
$\frac{\alpha + \mu_p^2/3k_B T}{3\epsilon_0}$	4.25×10^{-26}	2.08×10^{-28}	5.16×10^{-26}	4.52×10^{-28}

Polarizability α , permanent dipole moment μ_p , and the term $(\alpha + \mu_p^2/3k_B T)/3\epsilon_0$ of each ligand with and without Ag atoms bonded to the ligands are calculated.

AgMy and AgSC is evaluated by the Langevin–Debye formula:²²

$$P = \frac{N_m \mu_p^2 E}{3k_B T} + N_m \alpha E = 3\epsilon_0 \frac{\epsilon_r - 1}{\epsilon_r + 2} E, \quad (8)$$

$$\frac{\epsilon_r - 1}{\epsilon_r + 2} = \rho_N \left(\frac{\alpha + \mu_p^2/3k_B T}{3\epsilon_0} \right), \quad (9)$$

where N_m , E , and ρ_N are number of molecules per volume, an electric field, and the molecular number density, respectively. Here, P and μ_p of each ligand with and without three Ag atoms bonded to the O or S atoms were calculated by first-principles calculations. However, the actual structure between the Ag nanoparticles is a much more complex interface. Thus, the relation between the dipole moments and the permittivity for the unit model is discussed by the form of the Langevin–Debye as a first approximation. Therefore, the understanding of the relation between the dipole moments and the permittivity at the interface by the Debye formula will be limited to a qualitative discussion. As a large value on the right side of Eq. (9) causes a large relative permittivity, ρ_N , α , and μ_p are the determining factors for

permittivity (see Supplementary Fig. 6). In the present study, the number of ligands on an Ag nanoparticle remains unchanged before and after the ligand displacement reactions, because the number of Ag atoms involved in bonding to a single ligand is the same for both ligands (Table 1). In addition, as aggregations of Ag nanoparticles after the ligand displacement reactions were never observed, the density of ligands on the surface of the Ag nanoparticle was not so different between AgMy and AgSC, meaning that α and μ_p are the critical factors causing the difference in the permittivity between AgMy and AgSC. The calculated α , μ_p , and the term $(\alpha + \mu_p^2/3k_B T)/3\epsilon_0$ of each ligand with and without Ag atoms are summarized in Table 1. In the case of pristine ligands without Ag atoms, the ratios of α , μ_p , and the term relating SC to that of My are 1.09, 1.10, and 1.21, respectively, indicating that both ligands have almost the same relative permittivity and refractive index ($\epsilon_r^{1/2}$), as mentioned above. On the other hand, the ratios increase to 1.14, 3.36, and 2.17 for ligands with Ag atoms. This result strongly suggests that the Ag atoms bonded to the ligands cause changes in the physical properties between AgMy and AgSC, i.e., smaller DOS resulting

in smaller induced dipole moment, smaller permanent dipole moment, and lower permittivity at the Ag-O interface than those at the Ag-S interface. These facts are consistent with the above speculations with Eqs. (6) and (7), and also with the experimental results discussed in Fig. 1; namely, the permittivity and the dipole moment of the Ag-O interface are smaller than those of the Ag-S interface.

In brief, these experimental and theoretical results make us conclude that Ag atoms result in the lower DOS at the metal–ligand interface of AgMy than that at the metal–ligand interface of AgSC because of the different chemical interactions between Ag-O and Ag-S; furthermore, the lower permittivity at the Ag-O interface than that at the Ag-S interface is finally caused by the lower induced and permanent dipole moments, which reflect the DOS at Ag-O interface. However, the wave function at the interface absolutely needs to correspond to the Fermi level so that the electrons at the interface behave as valence electrons involved in the permittivity. This chemically induced permittivity-change (CIP) due to the alteration in the DOS at the metal–ligand interface before and after ligand displacement can play a key role in determining the LSPR properties of Ag nanoparticles. As a higher permittivity around the nanoparticle surface generally results in redshift and a higher intensity in a plasmon resonance spectrum (see Supplementary Fig. 7)^{12,23}, the longer plasmon resonance wavelength of AgSC films compared with that of AgMy films can be accounted for by the Ag-S interface having a higher permittivity than that of the Ag-O interface. The microscopic interface properties finally determine the macroscopic properties, as shown in Fig. 1. As the CIP effect is caused by the electronic state at the interface between a metal nanomaterial and the surface molecules on that metal, these dependences of plasmon resonance wavelength on capping molecules are observed in isolated Ag nanoparticles in a solution and in films (see Supplementary Fig. 8). As these plasmon resonance energy shifts due to the surface molecules have not been well understood, excluding the case of a change in the electron density of the metal^{9,10}, the CIP effect can be one of the reasons for these plasmon resonance energy shifts. However, the lower intensity and significantly wider FWHM in the spectrum of AgSC films shown in Fig. 1g cannot be explained by only the CIP effect, indicating that other effects contribute to the difference in the plasmon resonance spectra of AgMy and AgSC. Thus, we finally discuss the CID effect on the present Ag nanoparticles.

CID effect on AgMy and AgSC. The binding energy between Ag and O atoms is lower than that between Ag and S atoms, because the Ag-O interface has a higher ionic bonding property than that of the Ag-S interface (see Supplementary Fig. 9)¹⁶. These interactions are consistent with the principle of hard and soft acids and bases. As the orbitals for covalent bonding at the metal–ligand interface increase the scattering rate of the free electrons that contribute to the LSPR, the CID effect in AgMy is predicted to be smaller than that in AgSC, resulting in higher intensity and narrower FWHM in the plasmon resonance spectrum of AgMy. Indeed, AgMy films show higher intensity and narrower FWHM, as shown in Fig. 1g. To examine the influence of the CID effect on the LSPR properties of each nanoparticle experimentally, the complex dielectric functions of each film were measured by ellipsometry.

Figure 4a shows the real parts ϵ_1 in the complex dielectric functions $\epsilon = \epsilon_1 + i\epsilon_2$ for each Ag nanoparticle film. The function characteristics seem to be mainly attributed to electrons accorded to Lorentz model, suggesting that the electrons behave as bound electrons. When analyzing the results with only the Lorentz model, the ϵ_1 properties of AgMy exhibit a longer mean free path

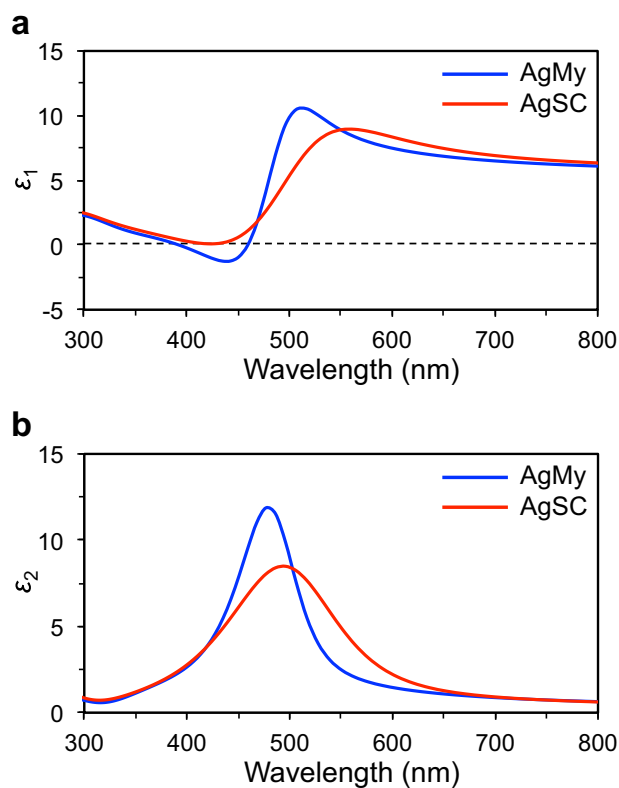


Fig. 4 Complex dielectric functions of AgMy and AgSC films measured by ellipsometry. **a** Real parts ϵ_1 of the complex dielectric function for AgMy (blue) and AgSC (red). Compared with that of AgSC, the ϵ_1 value of AgMy indicates a longer mean free path and smaller damping factor of the electrons that contribute to the LSPR; moreover, the electrons oscillating with the frequency corresponding to the negative value of ϵ_1 in AgMy can behave as free electrons without the CID effect. **b** Imaginary parts ϵ_2 of the complex dielectric function for AgMy (blue) and AgSC (red). The higher peak intensity of ϵ_2 for AgMy films indicates a higher conductivity of electrons oscillating as the LSPR in AgMy compared with that in AgSC.

and smaller damping factor of the electrons that contribute to the LSPR (see Supplementary Fig. 10)²⁴, compared with those of AgSC. As the Drude–Lorentz model is, however, an accurate model to explain the electrons that contribute to the LSPR in nanoparticles²⁵, it is important to analyze the results from the aspect of the Drude model, i.e., free electron behaviors. As pure Ag nanoparticles without ligands show a negative value of ϵ_1 in the visible region in the experimental and Drude models²⁶, the negative value of ϵ_1 for AgMy in the region of 393.7–459.3 nm implies that the electrons oscillating with this frequency in AgMy can behave as free electrons that are not affected by CID from the ligands (Fig. 4a). Interestingly, this negative ϵ_1 can be caused by the Ag-O interface, because AgSC and AgDT show only positive values of ϵ_1 (see Supplementary Fig. 11). Thus, these results suggest a smaller CID effect in AgMy than in AgSC, which is expected. Each imaginary part ϵ_2 in the complex dielectric functions is also consistent with the other results in this study. The peak intensity of ϵ_2 for AgMy films is larger than that of AgSC films (Fig. 4b). Here, the complex conductivity $\sigma = \sigma_1 + i\sigma_2$ depends on the complex dielectric function ϵ , which is described below,

$$\epsilon = 1 + i \frac{\sigma}{\omega \epsilon_0}, \quad (10)$$

where ω is the angular frequency of oscillating electrons. Then, the real part of the complex conductivity σ_1 is expressed as

$$\sigma_1 = \omega \epsilon_0 \epsilon_2. \quad (11)$$

The experimental result of the high peak intensity of ϵ_2 for AgMy films shown in Fig. 4b thus indicates the higher conductivity of electrons oscillating as the LSPR in AgMy compared with that in AgSC. In other words, the effective mean free path (l_{CID}) attributed to the CID effect in AgMy is longer than that in AgSC. As the CID effect (Γ_{CID}) can be described with the Fermi velocity v_F and l_{CID} ,

$$\Gamma_{\text{CID}} \propto v_F / l_{\text{CID}}, \quad (12)$$

a longer l_{CID} is equivalent to a smaller CID effect, thereby resulting in a larger intensity and narrower FWHM in a plasmon resonance spectrum.

In summary, the mechanisms and effects of a chemically induced change in the localized, induced, and permanent dipole moments at the metal–ligand interface on the LSPR properties of Ag nanoparticles were experimentally and theoretically examined in this study. The electron DOS at the metal–ligand interface was found to depend on the ligand. In addition, a smaller or larger DOS results in smaller or larger induced and permanent dipole moments, and finally a smaller or larger permittivity at the metal–ligand interface. However, it is noteworthy that the wave function at the interface absolutely needs to correspond to the Fermi level so that the electrons at the interface behave as valence electrons involved in the determination of the localized dipole moment. As the permittivity around the metal nanomaterial surface is one of the main determining factors of the LSPR properties of nanomaterials, this CIP due to surface molecules plays a key role in determining the LSPR properties. Indeed, this CIP effect is observed in other plasmonic nanoparticles (see Supplementary Figs. 12 and 13). Therefore, the CIP effect may be a novel factor for controlling the LSPR properties, thereby enabling us to design plasmonic materials and structures with more flexibility. Indeed, the combination of CID and CIP effects causes drastic changes in the plasmon resonance spectrum in the present Ag nanoparticle films, namely, an $\sim 47\%$ change, 93 meV shift, and 324 meV change in peak intensity, peak position, and FWHM, respectively. From the viewpoint of applied science, because the present results indicate the importance of the Fermi level of materials surrounding plasmonic nanomaterials in terms of LSPR properties, the final energy level alignment among the plasmonic nanomaterials, surrounding materials, and other materials used in an optoelectronics device would be important to design plasmonic matching. The findings presented here can contribute to the understanding of the interconnectedness between the electronic states at the metal–organic interface and the plasmonic properties of the metal from the perspectives of both fundamental materials science and applied science.

Methods

Preparations of Ag nanoparticles and Ag nanoparticle films. Ag nanoparticles (4.8 nm diameter) capped by myristate (AgMy) were synthesized by thermal decomposition method with silver acetate and myristic acid^{13,14}. AgMy nanoparticles dispersed in a mixture of toluene and ethanol were centrifuged at 6000 r.p.m. for 10 min at 15 °C, to remove unreacted excess myristic acid molecules, and toluene dispersion of AgMy nanoparticles was subsequently centrifuged at 15,000 r.p.m. for 10 min at 15 °C, to remove aggregates. The AgMy monolayer films were fabricated by Langmuir–Schaefer method with surface pressure of 15 mN m⁻¹, then the films were transferred onto a BK7 glass substrate for UV-visible absorbance spectrum measurements, a SiO₂ substrate for SEM observations, and a carbon grid for TEM observations. The reproducibility of the preparations of Ag nanoparticles and its films has been ensured by previous works^{16,27–29}. For AgSC and AgDT film preparations, AgMy films on each substrate were immersed into ethanol solution containing 1-tetradecanethiol (SC) or 1,16-hexadecanidithiol

(DT), respectively. The concentration of SC- and DT-ethanol solution was 1.7 mM and immersion time was 5 min, because this experimental condition was found to result in displacements of >85% ligands (from My to SC or DT) (see Supplementary Figs. 14 and 15)¹⁶.

Current–voltage measurements of Ag nanoparticle films. The gold interdigitated array electrodes with 20 μm space were fabricated on a SiO₂ substrate by photolithography for current–voltage (I – V) measurements. The substrates were cleaned by immersing into H₂SO₄ over 2 h and annealed over 6 h at 473 K in vacuum before transferring an AgMy film by Langmuir–Schaefer method. For Arrhenius plots, temperature dependences on I – V measurements were performed between -20 and 20 V under ultra-high vacuum condition and temperatures were controlled from 13 to 300 K by a cryostat (see Supplementary Fig. 16). Activation energies were estimated by fitting the Arrhenius plots in 100–300 K with Eq. (3).

First-principles calculations. To simulate the nanoparticle interfaces of AgMy and AgSC, density functional theory (DFT) calculations with periodic boundary conditions were carried out by using Vienna ab initio simulation package (VASP 5.4.1)³⁰. To model the nanoparticle surfaces, two Ag slabs exposing the (111) surface were constructed. The generated slabs have a 5×5 surface in the unit cell with a thickness of three atomic layers. They were placed parallel and spaced at a distance of 1.9 nm. Two My/SC molecules were placed between the two slab surfaces. In the direction perpendicular to the slab, a vacuum layer of 2 nm was inserted so that it can hinder the interaction between the junction structure and its replica in the neighboring cell. The molecule and the topmost layer of the Ag slab were allowed to relax in geometry optimization. The generalized gradient approximation was adopted with the functional described by Perdew, Burke, and Ernzerhof³¹. The Kohn–Sham equations were solved with a plane-wave basis set using the projector-augmented wave method^{32,33}. The cutoff energy for the plane-wave basis set was set to 450 eV. The break condition for the electronic self-consistent field loop was set to 1.0×10^{-5} eV. The force tolerance for the optimization of atomic positions was set to 0.05 eV \AA^{-1} . A Monkhorst–Pack k -point sampling of $2 \times 2 \times 1$ was used. For the dispersion correction, the Tkatchenko–Scheffler method³⁴ was adopted. The optimized structures were visualized by using VESTA³⁵. For the calculations of polarizability and dipole moment, the cluster model structures shown in Table 1 were cut out from the optimized slab model structures. A single point DFT calculation was carried out for each cluster model at the B3LYP level as implemented in the Gaussian 09 program³⁶. The LANL2DZ basis set was used for the Ag atom and the 6–31 G(d) basis set for the other atoms. The charge of the cluster without metal was set to -1 , whereas that of the model with metal was set to 0.

Data availability

The datasets that support the findings of this study are available from the corresponding authors upon reasonable request.

Received: 6 October 2020; Accepted: 6 May 2021;

Published online: 02 June 2021

References

- Watanabe, K., Menzel, D., Nilius, N. & Freund, H. J. Photochemistry on metal nanoparticles. *Chem. Rev.* **106**, 4301–4320 (2016).
- Foerster, B. et al. Interfacial states cause equal decay of plasmons and hot electrons at gold–metal oxide interfaces. *Nano Lett.* **20**, 3338–3343 (2020).
- Lan, X. et al. DNA-enabled chiral gold nanoparticle–chromophore hybrid structure with resonant plasmon–exciton coupling gives unusual and strong circular dichroism. *J. Am. Chem. Soc.* **141**, 19336–19341 (2019).
- Tauzin, L. J. et al. Exploring the relationship between plasmon damping and luminescence in lithographically prepared gold nanorods. *ACS Photonics* **5**, 3541–3549 (2018).
- Lee, S. Y. et al. Tuning chemical interface damping: interfacial electronic effects of adsorbate molecules and sharp tips of single gold bipyramids. *Nano Lett.* **19**, 2568–2574 (2019).
- Joplin, A., Hosseini et al. Correlated absorption and scattering spectroscopy of individual platinum-decorated gold nanorods reveals strong excitation enhancement in the nonplasmonic metal. *ACS Nano* **11**, 12346–12357 (2017).
- Hövel, H., Fritz, S., Hilger, A., Kreibitz, U. & Vollmer, M. Width of cluster plasmon resonances: bulk dielectric functions and chemical interface damping. *Phys. Rev. B* **48**, 18178–18188 (1993).
- Zijlstra, P., Paulo, P. M. R., Yu, K., Xu, Q. H. & Orrit, M. Chemical interface damping in single gold nanorods and its near elimination by tip-specific functionalization. *Angew. Chem. Int. Ed.* **51**, 8352–8355 (2012).
- Foerster, B. et al. Chemical interface damping depends on electrons reaching the surface. *ACS Nano* **11**, 2886–2893 (2017).
- Liyanage, T., Nagaraju, M., Johnson, M., Muhoberac, B. B. & Sardar, R. Reversible tuning of the plasmoelectric effect in noble metal nanostructures

- through manipulation of organic ligand energy levels. *Nano Lett.* **20**, 192–200 (2020).
11. Malola, S., Kappa, S. & Häkkinen, H. Role of nanocrystal symmetry in the crossover region from molecular to metallic gold nanoparticles. *J. Phys. Chem. C* **123**, 20655–20663 (2019).
 12. Olson, J. et al. Optical characterization of single plasmonic nanoparticles. *Chem. Soc. Rev.* **44**, 40–57 (2015).
 13. Abe, K. et al. Two-dimensional array of silver nanoparticles. *Thin Solid Films* **327–329**, 524–527 (1998).
 14. Keum, C. D. et al. A gram scale synthesis of monodispersed silver nanoparticles capped by carboxylates and their ligand exchange. *J. Nonlinear Opt. Phys. Mater.* **17**, 131–142 (2008).
 15. Chen, C. F., Tzeng, S. D., Chen, H. Y., Lin, K. J. & Gwo, S. Tunable plasmonic response from alkanethiolate-stabilized gold nanoparticle superlattices: evidence of near-field coupling. *J. Am. Chem. Soc.* **120**, 824–826 (2008).
 16. Saito, N., Wang, P., Okamoto, K., Ryuzaki, S. & Tamada, K. Large patternable metal nanoparticle sheets by photo/e-beam lithography. *Nanotechnology* **28**, 435705 (2017).
 17. Thomas, R. et al. Plexitons: the role of oscillator strengths and spectral widths in determining strong coupling. *ACS Nano* **12**, 402–415 (2018).
 18. Black, C., Murray, C., Sandstrom, R. & Sun, S. Spin-dependent tunneling in self-assembled cobalt-nanocrystal superlattices. *Science* **290**, 1131–1135 (2000).
 19. Andres, R. P. et al. Self-assembly of a two-dimensional superlattice of molecularly linked metal clusters. *Science* **273**, 1690–1693 (1996).
 20. Dayen, J. F. et al. Enhancing the molecular signature in molecule-nanoparticle networks via inelastic cotunneling. *Adv. Mater.* **25**, 400–404 (2013).
 21. Aleksandrovic, V. et al. Preparation and electrical properties of cobalt - platinum nanoparticle monolayers deposited by the Langmuir-Blodgett technique. *ACS Nano* **2**, 1123–1130 (2008).
 22. Atkins, P. & Paula, J. de. *Atkins' Physical Chemistry* 10th edn (OUP Oxford, 2014).
 23. Muskens, O., Christofilos, D., Del Fatti, N. & Vallée, F. Optical response of a single noble metal nanoparticle. *J. Opt. A Pure Appl. Opt.* **8**, S264–S272 (2006).
 24. Li, Y. In *Plasmonic Optics: Theory and Applications* (eds, Li, Y.) 19–23 (SPIE, 2017).
 25. Prokopidis, K. & Kalialakis, C. Physical interpretation of a modified Lorentz dielectric function for metals based on the Lorentz–Dirac force. *Appl. Phys. B Lasers Opt.* **117**, 25–32 (2014).
 26. Tolmachev, V. & Zharova, Y. Study of the optical properties of silver nanoparticle layers and Si-based nanostructure layers. *Phys. Stat. Solid. B* **254**, 1600758 (2017).
 27. Okamoto, K. et al. Tuning colors of silver nanoparticle sheets by multilayered crystalline structures on metal substrates. *Plasmonics* **8**, 581–590 (2013).
 28. Okamoto, K. et al. Electromagnetically induced transparency of a plasmonic metamaterial light absorber based on multilayered metallic nanoparticle sheets. *Sci. Rep.* **6**, 1–10 (2016).
 29. Wang, P. et al. Silver nanoparticles with tunable work functions. *Appl. Phys. Lett.* **107**, 1–5 (2015).
 30. Kresse, G. & Furthmüller, J. Efficiency of ab-initio total energy calculations for metals and semiconductors using a plane-wave basis set. *Comput. Mater. Sci.* **6**, 15–50 (1996).
 31. Perdew, J. P., Burke, K. & Ernzerhof, M. Generalized gradient approximation made simple. *Phys. Rev. Lett.* **77**, 3865–3868 (1996).
 32. Blöchl, P. E. Projector augmented-wave method. *Phys. Rev. B* **50**, 17953–17979 (1994).
 33. Kresse, G. & Joubert, D. From ultrasoft pseudopotentials to the projector augmented-wave method. *Phys. Rev. B* **59**, 1758–1775 (1999).
 34. Tkatchenko, A. & Scheffler, M. Accurate molecular van der Waals interactions from ground-state electron density and free-atom reference data. *Phys. Rev. Lett.* **102**, 073005 (2009).
 35. Momma, K. & Izumi, F. VESTA 3 for three-dimensional visualization of crystal, volumetric and morphology data. *J. Appl. Crystallogr.* **44**, 1272–1276 (2011).
 36. Frisch, M. J. et al. *Gaussian 09, revision E.01* (Gaussian, 2009).

Acknowledgements

This research is partially supported by the Japan Society for the Promotion of Science (JSPS) KAKENHI Grant Number 19K05234 and Japan Science & Technology Agency (JST) PRESTO Grant Number JPMJPR17HC. This work is also performed under the Cooperative Research Program of “Dynamic Alliance for Open Innovation Bridging Human, Environment and Materials.” Y.T. thanks Research Institute for Information Technology (Kyushu University) for the computational facilities and financial support from JSPS KAKENHI Grants JP19H04700 and JP20H04643. K.Y. thanks KAKENHI grants JP17K14440 and JP17H03117, MEXT projects of “Integrated Research Consortium on Chemical Sciences,” and “Elements Strategy Initiative to Form Core Research Center,” JST-CREST JPMJCR15P5, and JST-Mirai JPMJMI18A2. S.R. and Y.T. thank Institute for Materials Chemistry and Engineering (Kyushu University) for the financial support for young scientists.

Author contributions

N.S. and S.R. contributed equally. N.S. and S.R. planned and designed the study. N.S., S.R. and K.T. prepared Ag nanoparticles. N.S., S.R., Y.N. and R.M. obtained all experimental data. Y.T. and K.Y. obtained all theoretical data. N.S., S.R., Y.T., Y.N., P.W., D.T., Y.A. and K.O. performed data analyses. N.S., S.R. and T.Y. co-wrote the paper.

Competing interests

The authors declare no competing interests.

Additional information


Supplementary information The online version contains supplementary material available at <https://doi.org/10.1038/s43246-021-00159-6>.

Correspondence and requests for materials should be addressed to S.R. or K.T.

Peer review information: Primary handling editors: Reinhard Maurer, Aldo Isidori.

Reprints and permission information is available at <http://www.nature.com/reprints>

Publisher's note Springer Nature remains neutral with regard to jurisdictional claims in published maps and institutional affiliations.

 **Open Access** This article is licensed under a Creative Commons Attribution 4.0 International License, which permits use, sharing, adaptation, distribution and reproduction in any medium or format, as long as you give appropriate credit to the original author(s) and the source, provide a link to the Creative Commons license, and indicate if changes were made. The images or other third party material in this article are included in the article's Creative Commons license, unless indicated otherwise in a credit line to the material. If material is not included in the article's Creative Commons license and your intended use is not permitted by statutory regulation or exceeds the permitted use, you will need to obtain permission directly from the copyright holder. To view a copy of this license, visit <http://creativecommons.org/licenses/by/4.0/>.

© The Author(s) 2021